

## Aluminum cluster anions: Photoelectron spectroscopy and *ab initio* simulations

Jaakko Akola and Matti Manninen

*Department of Physics, University of Jyväskylä, FIN-40351 Jyväskylä, Finland*

Hannu Häkkinen and Uzi Landman

*School of Physics, Georgia Institute of Technology, Atlanta, Georgia 30332-0430*

Xi Li and Lai-Sheng Wang

*Department of Physics, Washington State University, Richland, Washington 99352*

*and W. R. Wiley Environmental Molecular Sciences Laboratory, Pacific Northwest National Laboratory,*

*MS K8-88, P.O. Box 999, Richland, Washington 99352*

(Received 11 April 2000)

Atomic structures and geometries, electronic structure, and temperature-dependent photoelectron spectra of  $Al_N^-$  ( $N=19-102$ ) clusters are studied both theoretically via *ab initio* local-density-functional simulations, and experimentally with high-resolution measurements. The use of a theoretically well-defined energy shift in conjunction with a generalized Koopmans' theorem enables direct comparisons between the calculated density of states and the experimental photoelectron spectrum. Such comparisons, using photoelectron spectra calculated for various relaxed cluster geometries, enables a determination of the optimal structures of the clusters. The atomic arrangements in the ground-state structures of  $Al_{19}^-$ ,  $Al_{20}^-$ , and  $Al_{23}^-$  are found and they exhibit oblate, prolate, and octupole deformed shapes, respectively. In addition to the low-temperature spectra, high-temperature calculated spectra of these clusters obtained via *ab initio* molecular-dynamics simulations reproduce the experimentally observed trends measured for hot clusters. For larger cluster anions ( $N \geq 36$ ), the level of agreement between the theoretically calculated spectra and the measured ones is less satisfactory, indicating that while certain structural motifs are identified, the optimal ground-state structures may not have been fully determined. fcc-like low-energy structures are found in the larger cluster-size range, with decreasing distortions of the internal structures when the cluster size is increased. Indications are found pertaining to an octahedral growth pattern of larger aluminum clusters.

### I. INTRODUCTION

The unique structures, stabilities, electronic and vibrational spectra, and thermal properties of clusters, and their size-dependent evolution, are main issues in cluster science. In particular, for simple metal clusters (e.g., *sp*-bonded materials), organization of the electronic energy levels into shells has been shown to play an important role in determining their size-evolutionary patterns.<sup>1</sup> Such shell models pertain to the formation of "magic number" sequences (that is, sequences of the numbers of electrons required to form closed electronic shells), correlating with enhanced energetic stability and a tendency towards (average) spherical cluster shapes for closed-shell clusters, as well as underlying shape deformations (away from spherical shape) for open-shell clusters.<sup>2</sup> While the original adoption of the nuclear shell model to explain magic number sequences observed in the abundance spectra of alkali-metal clusters has been based on a "jellium" mean-field picture,<sup>1,3</sup> the main features predicted by such models have been found often to maintain also, particularly (but not exclusively) under appropriate circumstances (e.g., simple metal clusters at sufficiently high temperatures), in more refined treatments where the atomic constituents were explicitly included in the calculations (see, e.g., Refs. 4 and 5).

Theoretical and experimental determinations of the ground state and isomeric geometrical structures (that is,

atomic arrangements) of clusters are still vexing and elusive issues. On the experimental side, the main problem originates from difficulties in applying common direct structure-determination techniques (e.g., x-ray or electron scattering) to such systems. Theoretical treatments of this issue are complicated by the complex nature of the multidimensional configurational free-energy surface of clusters, coupled with the propensity of such systems to form structural isomers that may dynamically interconvert at finite temperature. Additionally, the sensitivity of the electronic spectrum to the geometrical structure, and the interrelationship between the two, pose severe computational demands which until quite recently limited such investigations to rather small systems and mostly to static configurations.

Apart from clusters of alkali metals (Na and K in particular), aluminum clusters are perhaps the most extensively studied simple metal systems: such studies include experimental measurements of ionization potentials, electron affinities, photoelectron spectra, polarizabilities, and dissociation energies.<sup>6-10</sup> First-principles theoretical studies<sup>11-19</sup> have focused mainly (with a few exceptions<sup>17-19</sup>) on small-size aluminum clusters with up to  $\sim 20$  atoms because of computational demands. However, the emergence of high-performance computers and in particular parallel-computer platforms together with the development of new computational algorithms allow now extensive explorations of the properties of larger cluster sizes, and probing one of the main

questions in cluster research pertaining to the “convergence” with increasing cluster size of the structures of clusters to that of the bulk [face-centered cubic (fcc) for aluminum].

A few investigations have been reported on larger aluminum clusters,<sup>17–19</sup> and they focused mainly on clusters with “geometrically magic” numbers of atoms, that is, clusters comprised of 19 atoms (octahedron and double icosahedron), 43 atoms (octahedron), 55 atoms (icosahedron and cubo-octahedron), and 147 atoms (icosahedron and cubo-octahedron). A general conclusion which may be drawn from these studies is that with increasing cluster size the fcc-based (cube-)octahedral isomers become energetically favorable with respect to the corresponding icosahedral ones. In addition, in simulations performed for  $Al_N$  ( $N=12–23$ ) clusters,<sup>13</sup> comparisons were made between the icosahedral, decahedral, and octahedral isomers in the size range  $N=18–23$ .

Here we report on studies of  $Al_N^-$  ( $N=19–102$ ) clusters, using the method described by us recently<sup>14</sup> for theoretical simulations of the photoelectron spectra (PES) of cluster anions. In that study<sup>14</sup> we determined, through comparisons between calculated and measured PES spectra for  $Al_N^-$  ( $N=12–15$ ) clusters, the ground-state geometrical structures, and simulated the PES at both low and high temperatures (thus providing also estimates of the temperature of the clusters in the experiment). The method used in our previous study, as well as in this paper, is based on calculations of the PES spectra of cluster anions (both for selected optimized static configurations as well as for cluster configurations generated in the course of finite-temperature *ab initio* MD simulations). As discussed by us before, and elaborated further in this paper, practical and reliable evaluation of the PES spectrum of a cluster anion can be achieved via density-functional calculations<sup>20</sup> of its density of states (DOS) in juxtaposition with a shift of the DOS by the asymptotic value of the exchange-correlation potential. This theoretically founded method for calculations of the PES spectra is based on a “generalized Koopmans’ theorem,”<sup>21</sup> and it alleviates the use of ad hoc shifts of the calculated DOS (Ref. 22) or (first-order) perturbative treatments.<sup>23</sup> Extending our calculations in this study to larger aluminum cluster anions ( $N=19,20,23,36,38,52,54,55,79,102$ ) allows us to probe systematically the effect of shell closings (both electronic and atomic shells) on the PES, as well as to identify the pattern of convergence of certain properties of the clusters to the aluminum fcc-bulk behavior.

The experimental method for generating Al cluster anions at different temperature regimes is described in Sec. II. In Sec. III, we discuss the theoretical method used by us for density-functional-theory (DFT) calculations<sup>20</sup> and the isomer-generating processes. Section IV starts with a discussion of the theoretical validity of the generalized Koopmans’ theorem (GKT) and of PES simulations in the context of DFT for *sp*-bonded (Al,Na) clusters. In Sec. IV, we discuss results for  $Al_{19}^-$ ,  $Al_{20}^-$ , and  $Al_{23}^-$  isomers including comparisons between simulated and experimental high-temperature PES. Section IV continues with a discussion of our results and PES simulations for  $Al_{36}^-$ ,  $Al_{38}^-$ , and  $Al_{55}^-$  isomers and ends with the results for octahedrally grown

$Al_{52}^-$ ,  $Al_{54}^-$ ,  $Al_{79}^-$ , and  $Al_{102}^-$  fcc isomers. We summarize our findings in Sec. V.

## II. EXPERIMENT

The experiments were performed with a magnetic-bottle photoelectron apparatus equipped with a laser vaporization cluster source.<sup>24</sup> A pure aluminum disk target was vaporized by a pulsed laser beam (10 mJ/pulse at 532 nm). The laser-induced plasma was mixed with a helium carrier gas delivered by a dual-pulsed valve at a backing pressure of 10 atm. The clusters entrained in the carrier gas underwent a supersonic expansion to form a collimated beam by a skimmer. Negatively charged Al cluster ions were extracted perpendicularly into a time-of-flight mass spectrometer. The clusters of interest were size-selected, decelerated, and detached using an ArF excimer laser (193 nm, 6.424 eV). The photoelectrons were collected at  $\sim 100\%$  efficiency by the magnetic bottle and analyzed with a 3.5-m-long time-of-flight tube. The electron energies were calibrated by the known spectrum of  $Cu^-$ .

The reported binding-energy spectra were obtained by subtracting the kinetic energy spectra from the photon energy. In these experiments, the resolution was better than 30 meV for 1-eV electrons, which is superior to that measured previously for  $Al_N^-$  clusters (presumably hot) in the small-size range.<sup>9</sup> Significant temperature effects were observed in the photoelectron spectra of the aluminum clusters; the detailed temperature studies have recently been presented elsewhere.<sup>14,25</sup> Clusters leaving the nozzle early (short residence time) are expected to be quite hot, whereas clusters leaving the nozzle late (long residence time) are expected to be relatively cold. Indeed, based on *ab initio* molecular-dynamics simulations<sup>14</sup> of the PES spectra of  $Al_N^-$  with  $12 \leq N \leq 15$ , we deduced that the temperature of cold clusters is around 200 K, due to the supersonic cooling. PES spectra from such cold clusters usually exhibited well-defined spectral features representing the energy levels of the neutral clusters, while considerably broader spectra were obtained for hot clusters, whose temperature was estimated theoretically to be beyond 900 K.<sup>14</sup>

## III. THEORETICAL METHOD

The calculations were performed using the BO-LSD-MD (Born-Oppenheimer local-spin-density molecular-dynamics) method developed by Barnett and Landman.<sup>20</sup> In this method, the ions move according to classical molecular dynamics, with the electronic Hellmann-Feynman forces evaluated at each time step via a self-consistent solution of the Kohn-Sham (KS) equations, using the LSD approximation for the exchange correlation energy (with the exchange-correlation after Ref. 26), in conjunction with nonlocal norm-conserving pseudopotentials.<sup>27</sup> We note here that inclusion of the the gradient-corrections (GGA) after Ref. 28, while yielding better (lower) binding energies of the clusters compared to the experimental photodissociation data,<sup>8</sup> turned out to have a minimal effect on the structures as well as on the simulated PES and were not systematically used to produce the spectra.

An important element of the BO-LSD-MD method,<sup>20</sup> dis-

tinguishing it from those used previously in PES studies,<sup>22,23</sup> is the fact that it does not employ supercells (periodic replicas of the system), and consequently charged systems as well as those having permanent and/or dynamically developed multipole moments are simulated accurately in a straightforward manner on equal footing with neutral ones (i.e., alleviating the need for an artificial neutralizing background, large calculational cells, and/or approximate treatment of long-range multipole interactions).

The optimal cluster geometries and the corresponding energies were determined using a steepest-descent-like total energy minimization without any symmetry constraints. Most of the initial structures for this minimization were generated using a classical EMT (“effective medium theory”) potential.<sup>29</sup> In addition, we used also *ab initio* molecular dynamics in conjunction with simulated annealing. By optimizing configurations corresponding to local potential energy minima observed during such *ab initio* MD simulations, we were able to obtain additional low-energy isomers. Furthermore, lattice-based fcc isomers, which had a maximal coordination number, were generated for larger cluster sizes ( $N \geq 36$ ) using Monte Carlo (MC) simulations and a Metropolis algorithm.<sup>30</sup>

## IV. RESULTS

### A. Simulation of the experimental PES

It is well known that in the density-functional theory the auxiliary Kohn-Sham states are not necessarily the “true” molecular orbital levels of the system. However, according to Janak’s theorem,<sup>31</sup> there is a well-defined relationship between the ionization potential  $I(N_e)$  ( $N_e$  is the number of electrons in the system) and the energy eigenvalue  $\epsilon_{\text{HOMO}}(N_e)$  of the highest occupied KS state [i.e., the highest occupied molecular orbital (HOMO)]. Indeed, by either following Janak’s theorem<sup>31,32</sup> or via studying the asymptotic properties of the KS equation,<sup>21,33</sup> one can obtain a “generalized Koopmans’ theorem” (GKT), which states that

$$\epsilon_{\text{HOMO}}(N_e) - v_{\text{xc}}^{\infty}(N_e) = -I_{\text{GKT}}(N_e), \quad (1)$$

i.e., the energy eigenvalue of the highest occupied state has to be shifted by the asymptotic ( $r \rightarrow \infty$ ) limit of the exchange-correlation potential  $v_{\text{xc}}^{\infty}(N_e)$ , in order to obtain the ionization potential (the same idea applies of course also to the detachment energy). This shift is needed to correct both the electron self-interaction effects and the inaccuracies introduced by the continuous nature of the density functional.<sup>33</sup>

Although one can obtain the vertical detachment energy (vDE) rigorously by calculating the total energy difference between the anion and the photodetached (unrelaxed) neutral cluster, we wish here, for practical reasons, to make use of Eq. (1). In our earlier studies for Al and Na clusters, we have observed that the energy shift  $v_{\text{xc}}^{\infty}(N_e) = E(N_e - 1) - E(N_e) + \epsilon_{\text{HOMO}}(N_e)$  is practically constant for a certain cluster size regardless of the geometry of the cluster.<sup>14,32,34</sup> This allows us to use the same energy shift for a set of different isomers after we have calculated the mean value of  $v_{\text{xc}}^{\infty}(N_e)$ . As a result, we can determine the detachment energy distribution for a whole finite-temperature *ab initio* MD run, by shifting the recorded HOMO eigenvalue distribution (recorded along

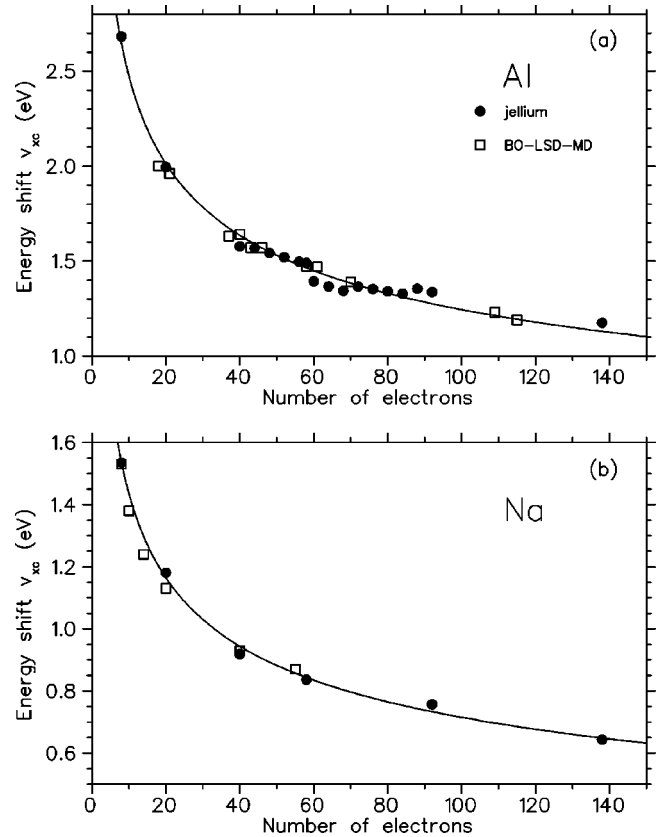


FIG. 1. The calculated energy shift  $v_{\text{xc}}^{\infty}$  as a function of valence electron number ( $N_e$ ) for (a) aluminum and (b) sodium clusters. The open squares correspond to the BO-LSD-MD results calculated (a) using the LSD approximation for  $N_e < 50$  and the LDA approximation for the larger electron numbers, and (b) using LDA approximation. The filled spheres correspond to the spherical jellium results calculated using the LDA approximation. The curves are fitted with respect to the jellium results.

the MD trajectories of the ions) by the calculated mean energy shift  $v_{\text{xc}}^{\infty}(N)$ ,<sup>32</sup> that is, the vDE is calculated as  $-\epsilon_{\text{HOMO}} + v_{\text{xc}}^{\infty}$  (this procedure neglects hole-relaxation effects).

Mean values of  $v_{\text{xc}}^{\infty}$  for Al and Na clusters calculated with the use of the BO-LSD-MD method are presented in Fig. 1. Included also are values obtained using the spherically constrained jellium model. The curves  $y = cx^{\alpha}$  [ $\alpha(\text{Al}) = -0.299$  and  $\alpha(\text{Na}) = -0.303$ ] are fitted to the jellium results [ $r_s(\text{Al}) = 2.07a_0$  and  $r_s(\text{Na}) = 3.93a_0$ ]. We observe that the BO-LSD-MD and jellium results are quite similar although the values for the ionization potential are known to differ considerably between these two models. We also note that to a reasonable accuracy,  $v_{\text{xc}}^{\infty} \propto N^{-1/3} \propto R^{-1}$  ( $R$  is the mean radius of the cluster).

So far we have only considered the HOMO states. While this procedure could be repeated to determine  $v_{\text{xc}}^{\infty}$  values for vDE’s from deeper (lower-energy) KS states, we have chosen to use a simpler (and more practical) procedure, whereby we use the shift calculated for the HOMO level also for deeper states. Indeed, in an earlier study,<sup>14</sup> we have shown that the same energy shift  $v_{\text{xc}}^{\infty}$  could be used with a satisfactory accuracy also for the inner (lower-energy) KS states of the cluster anions in order to get the correct electron detach-

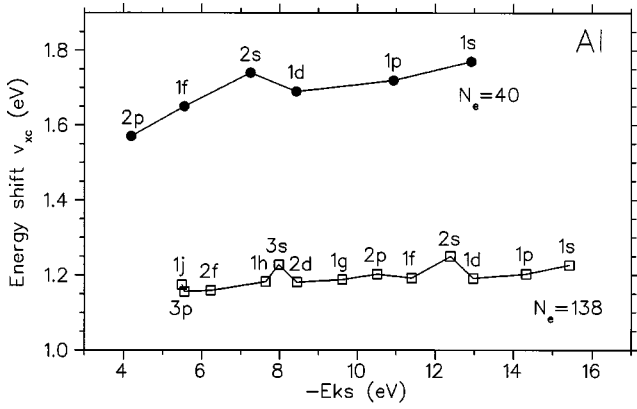


FIG. 2. The energy shift  $v_{xc}^{\infty}$  for different electron shells calculated using the spherical jellium model. The upper and lower curves correspond to the 40 and 138 valence electron aluminum systems, respectively.

ment energies for valence electrons below the HOMO, which we need in order to simulate the complete PES spectrum. This behavior is presented in Fig. 2, where the energy shifts  $v_{xc}^{\infty}$  are plotted for the inner single-particle states as a function of eigenenergies. These results were obtained using the restricted (spherical) jellium model for 40- and 138-electron aluminum systems and by calculating the total energy differences between the neutral cluster and the corresponding ion, where the electron is removed from the single-particle level in question. It is evident that for both cases shown in Fig. 2, the  $v_{xc}^{\infty}$  values for different orbitals are very close to each other: for the 40-electron systems the deviation is less than 0.2 eV while for the 138-electron systems it is only 0.1 eV. We note the mild increase in  $v_{xc}^{\infty}$  for the inner (lower-energy) KS states for both of these systems. Included also in Fig. 2 are the quantum numbers corresponding to the different orbitals, and we note that the  $s$  states tend to have locally larger  $v_{xc}^{\infty}$  values.

With the above we can now determine also the innercore detachment energies for the cluster anion isomers, and thus we can make direct comparisons between the experimental PES and the shifted DOS calculated for the corresponding cluster size. The finite width of the peaks of the PES is mainly due to the (finite) temperature (thermal motion of the ions), which causes the single-electron eigenvalues to fluctuate through coupling to the ionic motion.<sup>32</sup> At low temperatures a harmonic approximation is adequate and it leads to a Gaussian distribution of the single-particle levels. In practice, we plot the Gaussian-broadened DOS (shifted as discussed above by the mean value of  $v_{xc}^{\infty}$ ). Comparison of the theoretically simulated PES to the measured ones is expected to apply mainly to the location and line shapes (mainly width) of the peaks in the spectrum corresponding to the electron detachment energies, and the agreement between the measured and calculated PES is expected to improve for (energetically) optimal structures of the clusters. The relative intensity of the peaks in the PES spectrum may deviate, however, from the measured ones since our model does not take into account the different detachment cross sections of single-particle states. At elevated temperatures, the cluster may sample several isomeric configurations and, conse-

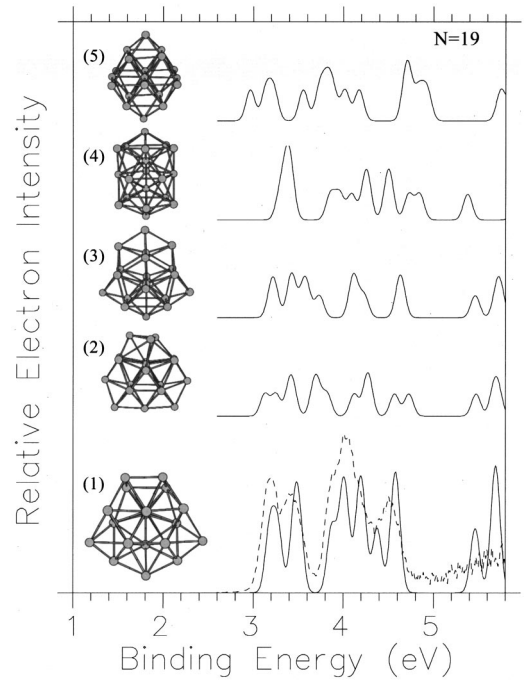


FIG. 3.  $Al_{19}^-$  isomers in energetic order and their simulated PES compared to the experimental high-resolution PES (dashed line) measured with a 193-nm laser in the cold temperature regime (long residence time). The theoretical PES were obtained by broadening the calculated DOS by 0.13 eV FWHM Gaussian and shifting the resulting distribution by the calculated  $v_{xc}^{\infty} = 1.47$  eV. The scaling of the intensity between the theoretical and experimental PES is arbitrary.

quently, at higher temperatures the PES are evaluated with the use of *ab initio* MD simulations (that is, along the ionic trajectories).

### B. $Al_{19}^-$ , $Al_{20}^-$ , and $Al_{23}^-$ isomers

Results for the structures of  $Al_{19}^-$  isomers and their calculated PES are presented in Fig. 3 along with the experimental high-resolution PES. Pertinent structural and energetic properties of these isomers are given in Table I. Here and in the following the isomers of  $Al_N^-$  for a given size ( $N$ ) are ordered according to their energetic stability, with

TABLE I. Properties of different  $Al_{19}^-$  isomers: total energy difference ( $\Delta E$ ) to the lowest energy isomer, HOMO-LUMO gap ( $E_g$ ), vertical detachment energy (vDE), mean nearest-neighbor distance ( $\langle d \rangle$ ), and the ratio between the two nondegenerate eigenvalues of the inertia tensor ( $\delta_I$ ). Energies in eV and distances in Å. In addition,  $\Delta E$  is also given in terms of temperature (in degrees K) by using the equipartition theorem:  $T = 2E/(3N-6)k_B$ , where  $N$  is the number of atoms in the cluster and  $k_B$  is the Boltzmann constant.

Isomer	$\Delta E$ (eV/K)	$E_g$ (eV)	vDE (eV)	$\langle d \rangle$ (Å)	$\delta_I$
19(1)	0.0	0.67	3.21	2.76	1.36
19(2)	0.045/21	0.71	3.15	2.74	1.32
19(3)	0.328/149	0.79	3.23	2.76	1.32
19(4)	0.392/178	0.53	3.28	2.79	0.68
19(5)	0.955/434	0.37	2.92	2.73	

TABLE II. The same as Table I, but for the  $\text{Al}_{20}^-$  isomers.

Isomer	$\Delta E$ (eV/K)	$E_g$ (eV)	vDE (eV)	$\langle d \rangle$ (Å)	$\delta_I$
20(1)	0.0	0.45	2.83	2.79	0.67
20(2)	0.617/265	0.15	2.82	2.76	0.78
20(3)	0.640/275	0.39	2.85	2.77	0.73
20(4)	0.935/402	0.49	3.22	2.82	
20(5)	1.246/535	0.11	2.78	2.77	

the lowest-energy isomer denoted as  $N(1)$ , the next higher-energy one as  $N(2)$ , and so on. The lowest-energy isomer 19(1) has an oblate shape with its internal structure having an icosahedral character. However, the top of the cluster exposes a four-atom (100) facet, reminiscent of the truncated decahedron. The higher-energy isomers 19(2) and 19(3) are also of oblate shape and their internal structure is decahedral. Indeed, these isomers can be obtained by removing atoms from a 23-atom decahedron. Isomer 19(4) is a prolate capped icosahedron; we note that due to its high coordination number this is the ground-state structure found by using the EMT potentials. Isomer 19(5) is a distorted octahedron, having an internal fcc-like structure (bulk Al).

The structural information given in Table I includes the average distance between the nearest neighbors,  $\langle d \rangle$ , and the ratio,  $\delta_I$ , between the nondegenerate eigenvalues of the inertia tensor in case two of them are (nearly) degenerate.<sup>35</sup> The average nearest-neighbor distances (2–4% less than the bulk value of 2.86 Å) are overall very similar for the  $\text{Al}_{19}^-$  isomers. In general, isomers with an icosahedral motif (which have the largest strain) tend to have a larger  $\langle d \rangle$  than the less strained decahedral and the strainless fcc isomers. The global shape of the cluster can be deduced from the ratio  $\delta_I$ : for  $\delta_I < 1$  the cluster is prolate and for  $\delta_I > 1$  it is oblate. As mentioned before, these isomers differ considerably from the spherical shape ( $\delta_I = 1$ ).

From Table I we note that the total energy difference between isomers 19(1) and 19(2) is rather small, while it is larger for the other isomers. Additionally, the energy gap between the highest occupied and the lowest unoccupied KS orbitals (HOMO-LUMO gap) and the vertical detachment energies vDE are quite large for these cluster anions. This result is consistent with the spherical jellium model, which predicts that a system of 58 valence electrons is magic; note, however, that these systems are far from being spherical.

Inspection of the theoretical PES and comparison with the measured one reveals that the PES for the 19(1) isomer (Fig. 3) agrees best with the experimental data. This agreement pertains to the locations of peaks and of the two main gaps in the experimental PES. Comparisons of the PES of the other structural isomers with the data show clear differences, suggesting that the experimental PES originates mainly from one specific isomer. The high sensitivity of the PES to the cluster geometry is quite evident; e.g., note the differences between the spectra corresponding to the 19(2) and 19(3) isomers, although the total shapes and internal structures of these clusters are rather similar.

Results for the  $\text{Al}_{20}^-$  isomers and their calculated PES are given in Table II and Fig. 4. The lowest-energy isomer 20(1) (see Table II) is prolate in shape and its internal structure is a hybrid of an icosahedral stacking and a hexagonal pyrami-

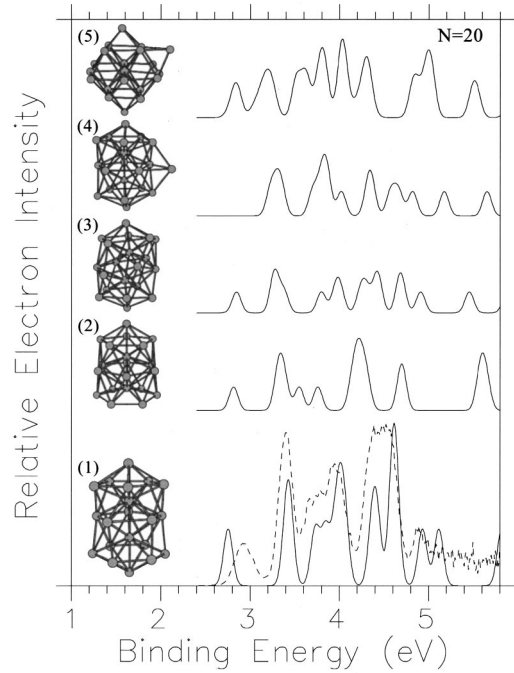


FIG. 4. The same as Fig. 3, but for the  $\text{Al}_{20}^-$  isomers.  $v_{xc}^\infty = 1.47$  eV.

dal one. This structure can be described as a 13-atom icosahedron (see the upper part of the cluster shown at the bottom of Fig. 4) situated on top of the base of an inverted hexagonal pyramid. The energetically closest isomer 20(2) has a similar structure to that of 20(1), with the central pentagon of 20(1) replaced by a hexagon, and the lowermost atom of 20(1) moved to another location in the cluster, thus causing the cluster's shape to be less prolate. The initial structure (before optimization) of 20(3) was constructed also to be similar to that of 20(1), with the bottom hexagon and the central pentagon of 20(1) switched, causing the initial structure to be very symmetric. However, during optimization the structure distorted drastically, yielding the prolate shape shown in Fig. 4. Isomer 20(4) is the 19-atom capped icosahedron with one extra atom; as was the case for  $\text{Al}_{19}^-$ , this isomer is the ground state for the EMT potential. Isomer 20(5) is a 19-atom (strongly distorted) octahedron capped by a single atom. As for the  $\text{Al}_{19}^-$  isomers, the average nearest-neighbor distances are similar for all the  $\text{Al}_{20}^-$  isomers with larger  $\langle d \rangle$  for the icosahedral one, 20(4), which is somewhat strained.

From Table II, we observe that the total energy of the 20(1) isomer is well below the energies of the other isomers, and that compared to the  $\text{Al}_{19}^-$  isomers the energy difference to the pure icosahedral and the octahedral structures is considerably larger. This could be related to the shapes of the clusters, since the lower-energy isomers 20(1)–20(3) have a prolate shape whereas the 20(4) and 20(5) isomers are triaxially deformed. The HOMO-LUMO gaps and the vDE's of the  $\text{Al}_{20}^-$  isomers are clearly smaller than those for the  $\text{Al}_{19}^-$  isomers, indicating some kind of shell closing between  $\text{Al}_{19}^-$  and  $\text{Al}_{20}^-$  (58 and 61 electrons, respectively); such shell closing is supported also by the behavior of the PES near threshold (compare Figs. 3 and 4, bottom curves).

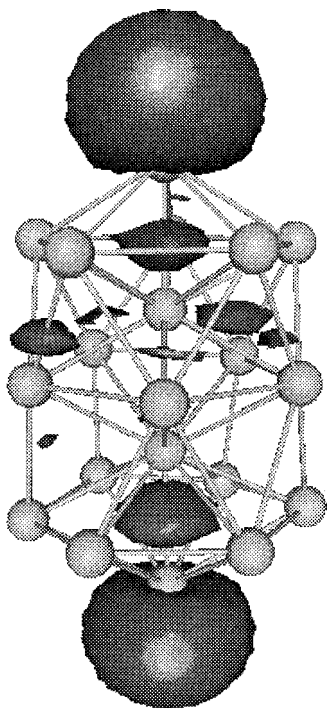


FIG. 5. The charge-density isosurface of the HOMO state of the lowest-energy isomer 20(1). The value of the density is  $-0.00066$  a.u. (7% of the maximum density) and the charge accumulated inside the isosurface is  $-0.48e$ .

As for the  $\text{Al}_{19}^-$  cluster, the PES corresponding to the energetically lowest-lying isomer of  $\text{Al}_{20}^-$  agrees best with the experimental data. However, the location of the first peak (and threshold) in the calculated PES is somewhat lower in energy than that in the experiment; this is most likely due to the use of the same  $v_{xc}^\infty$  for all the isomers as well as for all the KS single-particle orbitals, and it may also be related to the spatial nature of the HOMO orbital; see Fig. 5 where the isosurface of the HOMO electron density exhibits significant localization on the two outermost atoms of the cluster, unlike the delocalized nature of the orbitals of states below the HOMO level.<sup>36</sup>

Results for the  $\text{Al}_{23}^-$  cluster are given in Fig. 6 and Table III. The lowest-energy isomer 23(1) (see Table III) has an octupolar deformed shape with an internal structure of an unidentifiable motif; some resemblance to an octahedron with fcc stacking may be found. This isomer is quite similar to the isomer 23(3), whose initial structure (prior to optimization) was a capped octahedron; in fact, the 23(1) cluster was obtained via quenching during a high-temperature *ab initio* MD simulation starting from the 23(3) isomer. Isomers 23(2) (symmetric decahedron) and 23(5) (icosahedral) have a similar oblate shape. Isomer 23(4) is the icosahedral EMT ground state for  $\text{Al}_{23}$  and it too has an oblate global shape.

From Table III, it is seen that the total energy of the 23(1) cluster is well below the other isomers. Despite its totally different shape, the decahedron 23(2) is the next lowest isomer. It is evident that the icosahedral isomers 23(4) and 23(5) are energetically inferior. As for the preceding cluster sizes, the average nearest-neighbor distances  $\langle d \rangle$  are similar for all the isomers, and again the less strained structures tend to have a lower  $\langle d \rangle$ . However, isomer 23(5) is an exception

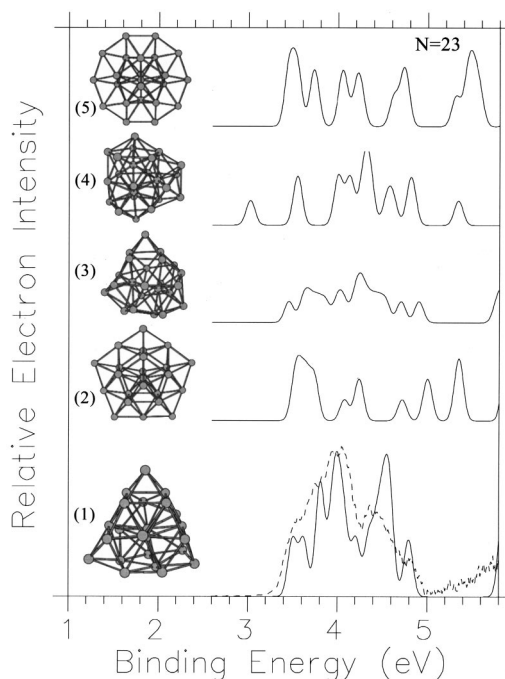


FIG. 6. The same as Fig. 3, but for the  $\text{Al}_{23}^-$  isomers.  $v_{xc}^\infty = 1.39$  eV.

to this behavior with an unusually small  $\langle d \rangle$  for an icosahedral structure. It is interesting, however, to note that this structure gives a much higher total energy than isomer 23(2), which has a similar global shape.

As for the  $\text{Al}_{19}^-$  and  $\text{Al}_{20}^-$  clusters, the PES corresponding to the energetically lowest isomer 23(1) gives the best agreement to the experimental measurement. The location of the “band” comprised of a number of peaks and the position of the gap opening at higher energy are correctly predicted (see Fig. 6). Not surprisingly, the PES for the isomer 23(3) yields a certain resemblance to the experimental data, while the other isomers exhibit totally different spectra.

Inspection of the measured PES (Ref. 10) indicates the occurrence of a shell closing between  $\text{Al}_{23}^-$  and  $\text{Al}_{24}^-$ , since the threshold of  $\text{Al}_{24}^-$  appears as a minor peak split from the main band (similar to the PES of  $\text{Al}_{23}^-$ ). This is in contradiction with the spherical jellium model, where 68 electrons is a magic number. We believe that the reason for the apparent shell closing after 70 electrons seems to be the octupole deformation.<sup>37–39</sup> This can be seen from Table III, where the octupole deformed isomers 23(1) and 23(3) are found to have high values for the HOMO-LUMO gap and the vDE. Also the oblate isomers 23(2) and 23(5) have considerable values for these quantities.

TABLE III. The same as Table I, but for the  $\text{Al}_{23}^-$  isomers.

Isomer	$\Delta E$ (eV/K)	$E_g$ (eV)	vDE (eV)	$\langle d \rangle$ (Å)	$\delta_I$
23(1)	0.0	1.07	3.54	2.75	$\approx 1$
23(2)	0.313/115	0.76	3.49	2.77	1.56
23(3)	0.506/186	1.01	3.45	2.75	$\approx 1$
23(4)	0.905/333	0.18	3.03	2.82	1.19
23(5)	1.763/649	0.86	3.44	2.72	1.59

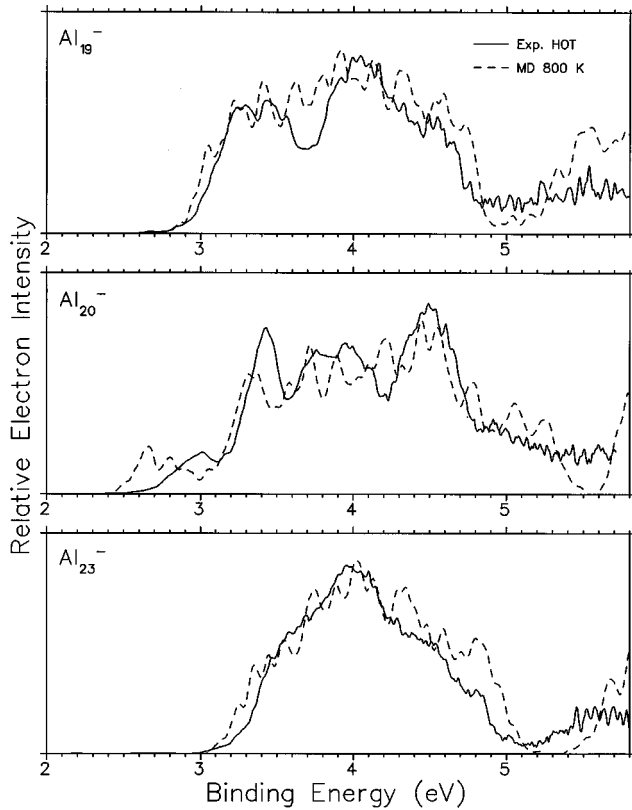


FIG. 7. Temperature-dependent PES for  $\text{Al}_{19}^-$ ,  $\text{Al}_{20}^-$ , and  $\text{Al}_{23}^-$  measured at the hot temperature regime (short residence time) with a 193-nm laser (solid lines) compared to the PES obtained from *ab initio* MD simulations at 800 K (dashed lines). The theoretical PES were obtained by broadening the recorded DOS with 0.05-eV FWHM Gaussian and shifting the resulting distribution by the calculated  $v_{xc}^\infty$ . The scaling of intensity between the theoretical and experimental PES is arbitrary.

We turn now to an analysis of the temperature dependence of the PES spectra. In Fig. 7, we present the PES of the  $\text{Al}_{19}^-$ ,  $\text{Al}_{20}^-$ , and  $\text{Al}_{23}^-$  cluster anions measured at the hot experimental regime; that is, when the nozzle residence time of the cluster jet was substantially shorter than for the clusters in the cold regime (i.e., the data shown in Figs. 3, 4, and 6). The experimental PES for each of the cluster sizes (temperature of the clusters unknown) is compared to that calculated during a 2.5-ps constant energy *ab initio* MD simulation (at an average temperature of 800 K) of the corresponding lowest-energy isomer [determined by us as discussed above through analysis of the PES spectra measured at the cold temperature regime, see isomers marked (1) in Figs. 3, 4, and 6]. The agreement between the theoretical predictions and the measured results is evident. The thermal effects are portrayed by the occurrence of a thermal tail near threshold, broadening of the main features, and smearing of the sharp details. However, the quality of agreement with the measurements, while quite satisfactory, is not as good as that shown above (Figs. 3, 4, and 6) for the measured PES from clusters generated at the cold regime (which were compared to the PES calculated for the lowest-energy isomers at 0 K). The remaining discrepancies between the measured and simulated PES in Fig. 7 are most certainly a consequence of the rather short simulation time, which does not allow a com-

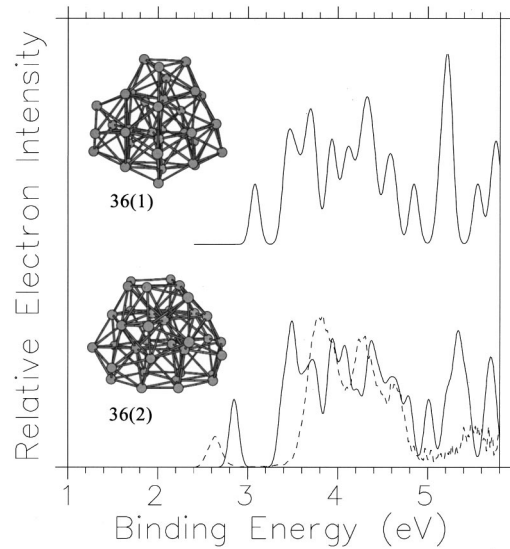


FIG. 8. The same as Fig. 3, but for the two lowest-energy isomers of  $\text{Al}_{36}^-$ . Note that the better agreement to the data is obtained here for the higher-energy isomer [36(2)].  $v_{xc}^\infty = 1.23$  eV.

prehensive sampling of the configuration space of the clusters; this, however, can be alleviated via longer simulations. From these results we may conclude<sup>14</sup> that temperature-dependent effects in the PES are dominated by the thermal motion of the ions, rather than by thermal excitations of the electrons whose contributions are negligible because of the considerable HOMO-LUMO gaps in these clusters (see Tables I–III).

### C. $\text{Al}_{36}^-$ and $\text{Al}_{38}^-$ isomers

The structures of the two lowest-energy isomers of  $\text{Al}_{36}^-$  and their corresponding calculated PES are shown in Fig. 8 along with the measured PES for  $\text{Al}_{36}^-$ ; note that the experimental data are superimposed here on the theoretical spectrum of the higher-energy isomer, 36(2), which is in better agreement with the data than the PES calculated for the 36(1) isomer. Certain energetic and structural properties of these isomers as well as for some other low-energy isomers are given in Table IV. Isomers 36(1) and 36(2) do not have an identifiable (internal) structural motif. Additionally, their overall shapes are not well-defined [particularly for the 36(1) structure]. It also seems that clusters at this size range start to exhibit clear surface facets; this can be seen most conveniently at the bottom part of the 36(2) isomer, where a distorted (111) facet can be identified.

The values of  $\langle d \rangle$  (see Table IV) are very similar for all the isomers and they approach the bulk crystalline fcc value (i.e.,  $\langle d \rangle$  in the clusters is shorter than  $\langle d \rangle_{\text{bulk}}$  by  $\sim 2-3\%$ ). The other higher-energy isomers listed in Table IV (not shown in Fig. 8) are of similar structural motif to the 36(1) and 36(2) isomers; they all have dense compact geometries with distorted internal structures, and most of them expose some (111)-type distorted facets. Isomer 36(6) differs from the other isomers by being an almost perfect fcc structure. In fact, this isomer was obtained by cutting off two atoms from a perfect 38-atom truncated octahedron and optimizing the resulting structure. We have also confirmed by performing a

TABLE IV. The same as Table I, but for the  $\text{Al}_{36}^-$  isomers. Additionally, we give the energy gap between the HOMO state and the closest underlying state ( $\Delta\epsilon$ ) and the vertical ionization potential (vIP) of the corresponding neutral isomer.

Isomer	$\Delta E$ (eV/K)	$E_g$ (eV)	$\Delta\epsilon$ (eV)	vDE (eV)	vIP (eV)	$\langle d \rangle$ (Å)	$\delta_l$
36(1)	0.0	0.40	0.34	3.07	5.81	2.77	1.10
36(2)	0.067/15	0.18	0.54	2.85	5.80	2.78	1.15
36(3)	0.106/24	0.27	0.48	2.91	5.81	2.78	1.14
36(4)	0.187/43	0.34	0.23	3.05	5.66	2.78	
36(5)	0.210/48	0.30	0.19	3.03	5.67	2.78	
36(6)	0.679/154	0.17	0.30	2.92	5.62	2.80	

Monte Carlo fcc-generation procedure<sup>30</sup> that this structure is also the most favorable 36-atom fcc structure with the optimal coordination number.

As seen from Fig. 8, we are not able to reproduce the experimental PES for the  $\text{Al}_{36}^-$  cluster as satisfactorily as for the smaller ones (see Figs. 3, 4, and 6). We believe that the reason is simply that we have not found here the correct optimal structure. However, we observe in the calculated spectrum the opening of a new shell ( $\text{Al}_{36}^-$  has 109 electrons) for most of the low-energy isomers (see Table IV). In particular, for the 36(2) isomer we note a sizable energy gap ( $\Delta\epsilon \sim 0.5$  eV, see Table IV) between the HOMO state and the underlying states, which is rather significant for such a large number of valence electrons; the experimental gap is even larger (see dashed-line curve in Fig. 8).

The charge-density isosurface for the HOMO-state of the isomer 36(2) is plotted in Fig. 9 with the cluster viewed from the top with reference to the orientation shown at the bottom of Fig. 8. It is evident that the charge of this orbital is delocalized on the exterior of the cluster in 12 ‘‘pockets.’’<sup>40</sup> Comparison to the underlying states shows that these states have a clearly different nature—specifically, they are strongly spread over the whole cluster, with a considerable part of their charge density found inside the cluster. This

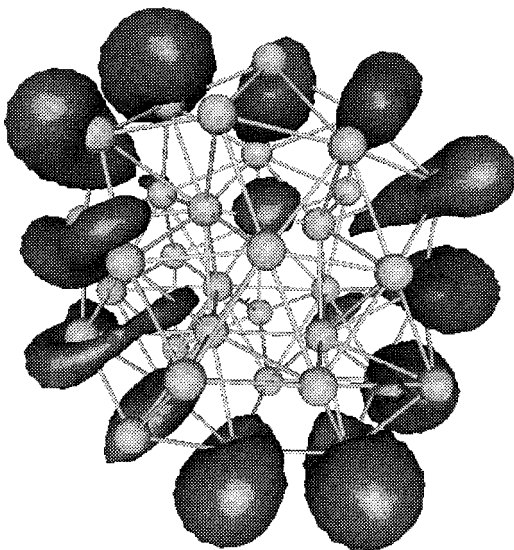


FIG. 9. The charge-density isosurface of the HOMO state of the low-energy isomer 36(2). The value of the density is  $-0.00036$  a.u. (corresponding 9% of the maximum density) and the charge accumulated inside the isosurface is  $-0.57e$ .

difference in orbital character correlates with the large energy gap between the HOMO state and the underlying states in the theoretical PES.

In addition to the HOMO-LUMO gaps,  $E_g$ , and the vDE, we give in Table IV the values of the gap,  $\Delta\epsilon$ , between the HOMO state and the closest underlying state, and of the vertical ionization potential (vIP) for the corresponding optimized neutral cluster. From these results we observe that the range of values of the HOMO-LUMO gap and of  $\Delta\epsilon$  is almost the same. This indicates that the HOMO state is separated from the other occupied states for all these isomers and it supports the conclusion pertaining to the opening of a new shell, as discussed above in the context of the PES. The vDE and vIP values have a slight (0.2 eV) variation among the different isomers. As seen from the experimental PES, the vDE values are over 0.3 eV too large (the experimental value for the first peak is 2.63 eV). The IP thresholds for  $\text{Al}_N$  clusters (up to  $N=70$ ) have been measured,<sup>6</sup> and they exhibit a peculiar double-threshold effect for cluster sizes in the range of  $N=36-42$ . Consequently, two IP values were reported<sup>6</sup> for  $\text{Al}_{36}$ : 5.20 and 5.50 eV. It is evident that the isomers observed in this study do not correspond to the lower threshold. However, the upper threshold is in the correct position, if we assume that the thermal effects lower the threshold slightly from the theoretical vIP values.<sup>32</sup>

Two low-energy isomers of  $\text{Al}_{38}^-$  and their theoretical PES, as well as the measured spectrum, are shown in Fig. 10. The isomers that we show here are the lowest-energy one, 38(1), and isomer 38(4), which yielded the best agreement between the theoretical PES and the data, particularly with respect to the threshold region of the experimental PES. Some of the properties of these and other low-energy isomers are presented in Table V. Similar to the  $\text{Al}_{36}^-$  isomers, isomers 38(1) and 38(4) have a distorted internal structure. However, now it seems possible to identify the corresponding internal structural motif, with isomer 38(1) exhibiting a decahedral pattern (pentagon in the middle of cluster) and isomer 38(4) showing a fcc structural pattern. Both of these isomers are prolate. The geometries of other low-energy isomers (not shown in Fig. 10) are closely related to these two isomers; both decahedral and fcc patterns can be identified and the shape parameters  $\delta_l < 1$  imply a prolate deformation. Isomer 38(6) is an optimized truncated octahedron which maintained its fcc-structure during the optimization (with some elongation of the structure). The values of the nearest-neighbor distance  $\langle d \rangle$  are very similar to the  $\text{Al}_{36}^-$  results and they are rather close to the fcc-bulk value (see Table V).

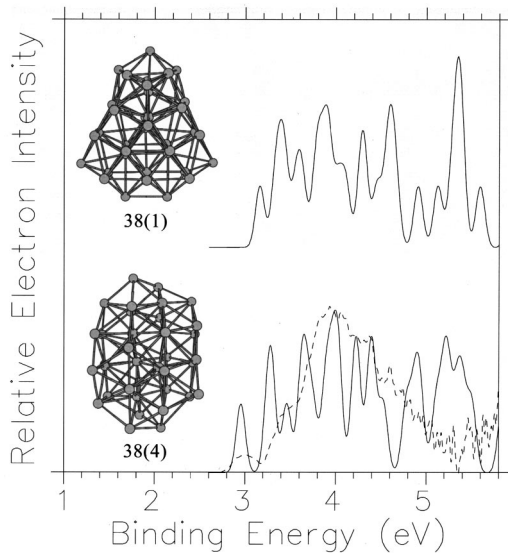


FIG. 10. The same as Fig. 3, but for the two low-energy isomers of  $\text{Al}_{38}^-$ .  $v_{xc}^\infty = 1.19$  eV.

The distribution of distance between the ions in the isomer 38(4) are shown in Fig. 11, with the arrows marking the positions of neighbor distances in the bulk fcc crystal. We observe that the distances are distributed smoothly over the whole interval 2.4–10 Å. However, despite the distorted geometry of the cluster, one can relate many of the peaks of the histogram to the fcc-bulk values (the tendency for shrinkage of interatomic distances in the finite cluster compared to the bulk should be taken into account). On the basis of above, we conclude that the structure of isomer 38(4) resembles fcc stacking although it is considerably distorted. This applies for most of the  $\text{Al}_{36}^-$  and  $\text{Al}_{38}^-$  low-energy isomers found by us.

From comparison of the calculated PES with the measured one, we conclude that while the PES of isomer 38(4) exhibits the right threshold behavior, the overall agreement for the rest of the spectrum is less satisfactory. The reason for the discrepancy is that we may not have found the optimal cluster geometry because of the large number of different possible configurations and complicated distorted internal structures of clusters in this size range. Nevertheless, we are now able to show the new shell opening after 114 electrons ( $\text{Al}_{38}^-$  has 115 electrons) in the correct location (see the region near 3.1 eV in Fig. 10).

Table V contains information about the shell opening, correlating with that found from Fig. 10 since the values of  $\Delta\epsilon$  are within 0.2–0.3 eV, which is similar to the “gap” in the PES near the threshold. The values of the HOMO-

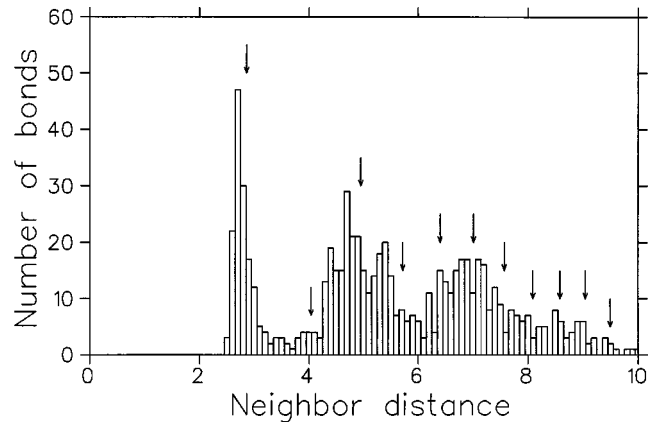


FIG. 11. Histogram of the distances (in Å) between the ions in the 38(4) isomer. The arrows correspond to the crystalline fcc-bulk distances.

LUMO gap  $E_g$  are also in the same range. Contrary to the  $\text{Al}_{36}^-$  results, the calculated vDE values are now closer to the experimental value (3.00 eV) of the first peak. The vIP values are in the same range as for  $\text{Al}_{36}^-$  although the deviation is now smaller (0.1 eV). The experimental values for the IP threshold are 5.20/5.45 eV (Ref. 6) and 5.25 eV (lower bound from Ref. 41). Accordingly, our results correspond to the upper threshold reported in Ref. 6, if a slight thermal lowering of the threshold is invoked.

#### D. $\text{Al}_{52}^-$ , $\text{Al}_{54}^-$ , $\text{Al}_{55}^-$ , $\text{Al}_{79}^-$ , and $\text{Al}_{102}^-$ isomers

The structures of two of the lowest-energy  $\text{Al}_{55}^-$  isomers and their theoretical PES compared to the experiments are presented in Fig. 12, with the measured spectrum superimposed on that of isomer 55(3), which yielded the best agreement to the data. Some physical properties of these and other isomers which we studied are listed in Table VI. The initial structure of isomer 55(1) before optimization was obtained by a Monte Carlo fcc-generating procedure,<sup>30</sup> where the coordination number of the cluster is maximized [causing the cluster to have mainly close-packed (111) facets]. The LDA-based optimization did not introduce significant changes to this geometry. Isomer 55(2) (not shown) was obtained in a similar way and it has the same coordination number as 55(1). Isomer 55(3) is an optimized structure starting from an EMT-generated distorted structure, and it has one preferred deformation axis. By viewing the cluster from the top with respect to the orientation shown in Fig. 12, one observes that the cluster shape is hexagonal, which implies that the cluster resembles fcc stacking. Isomer 55(4) is a decahedron, which has deformed to a strongly prolate shape. The

TABLE V. The same as Table IV, but for the  $\text{Al}_{38}^-$  isomers.

Isomer	$\Delta E$ (eV/K)	$E_g$ (eV)	$\Delta\epsilon$ (eV)	vDE (eV)	vIP (eV)	$\langle d \rangle$ (Å)	$\delta_I$
38(1)	0.0	0.34	0.17	3.18	5.69	2.79	0.80
38(2)	0.084/18	0.25	0.18	3.05	5.65	2.79	0.72
38(3)	0.205/44	0.24	0.22	3.06	5.68	2.78	0.73
38(4)	0.247/53	0.20	0.30	2.96	5.66	2.78	0.74
38(5)	0.318/68	0.28	0.24	3.10	5.68	2.78	0.74
38(6)	0.905/194	0.07	0.27	2.90	5.63	2.82	0.91

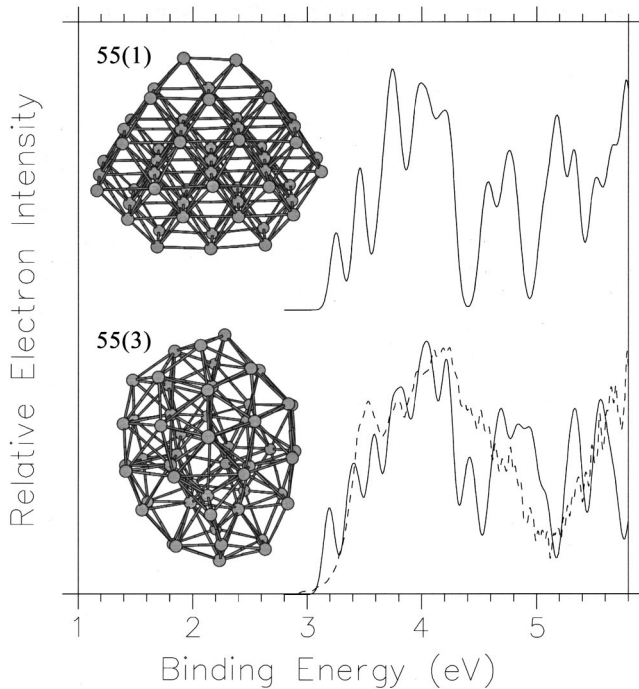


FIG. 12. The same as Fig. 3, but for the two low-energy isomers of  $\text{Al}_{55}^-$ .  $v_{xc}^\infty = 1.08$  eV.

internal structure of this cluster has, however, maintained the decahedral motif. Isomer 55(5) is another EMT-generated isomer, which is strongly triaxially deformed. The internal structure of this isomer is a hybrid of a decahedral structure and fcc stacking. The nonoptimized starting structures of isomers 55(6) and 55(7) were a perfect icosahedron (EMT ground state) and cubo-octahedron, respectively. Both these isomers distorted significantly during optimization, which leads us to a conclusion that the 55-atom icosahedron and cubo-octahedron are unstable isomers for  $\text{Al}_{55}^-$ .

While a comparison between the PES calculated for the 55(3) isomer with the experimental data shows overall a relatively satisfactory level of agreement (Fig. 12), particularly with respect to the locations of the main peaks, certain sharp details observed in the experimental PES are not reproduced by the calculation. These discrepancies could be due to an incomplete structural optimization.

An issue of great interest in studies of clusters is that pertaining to the convergence of the structure of clusters to

the bulk structural motif (fcc for Al). Indication about the onset of such convergence may be obtained here by noting from Table VI that the fcc-like structures of isomers 55(1) and 55(2) are indeed the lowest-energy ones; the average nearest neighbor  $\langle d \rangle$  in the  $\text{Al}_{55}^-$  isomers is very close to the Al bulk fcc value (2.86 Å, see Table VI). However, we remark that the competition in this size range from highly distorted or non-fcc structural forms is still strong (see Table VI). This may be related to the still large surface-to-volume ratio for the 55-atom clusters and the destabilizing effect of corner and edge atoms in the 55(1) and 55(2) isomers. With further increase in cluster size, the relative contribution from such undercoordinated atoms will decrease, stabilizing the bulk structural motif. We note here that neither the icosahedron nor the cubo-octahedron-based (distorted) structures [isomers 55(6) and 55(7)] are competitive for  $\text{Al}_{55}^-$ ; this is most likely because of the accumulated icosahedral strain and the large high-surface energy (100) facets in the cubo-octahedron, respectively.

The energetic properties of the  $\text{Al}_{55}^-$  isomers are rather similar (see Table VI). For all these isomers, the values of the HOMO-LUMO gap  $E_g$  are in the range of 0.2–0.3 eV (which is in the same size range as for the  $\text{Al}_{36}^-$  and  $\text{Al}_{38}^-$  isomers) and the vDE values (corresponding to the first peak of the PES) are in the range of 3.2–3.4 eV, in agreement with the threshold of the experimental PES around 3.0–3.2 eV (see Fig. 12). The vIP values of the different isomers are also quite similar to each other. As for the  $\text{Al}_{36}^-$  and  $\text{Al}_{38}^-$  isomers, the theoretical vIP values are 0.2–0.4 eV too large with respect to the experimental threshold values [5.01 eV (Ref. 6) and 5.04 eV (Ref. 41)].

Finally, we present in Table VII certain physical properties of the fcc-generated  $\text{Al}_{52}^-$ ,  $\text{Al}_{54}^-$ ,  $\text{Al}_{79}^-$ , and  $\text{Al}_{102}^-$  isomers. The coordination number of these isomers is maximized using the Monte Carlo procedure resulting in large (111) facets for each of the clusters. The structures of  $\text{Al}_{52}^-$  and  $\text{Al}_{54}^-$  resemble closely that of the 55(1) isomer shown in Fig. 12, and they may indeed be obtained from this isomer by removing the less coordinated corner and edge atoms.  $\text{Al}_{79}^-$  is a truncated octahedron and  $\text{Al}_{102}^-$  is built by adding two neighboring (111) facets to the  $\text{Al}_{79}^-$  cluster. It is worthwhile mentioning that the  $\text{Al}_{52}^-$  and  $\text{Al}_{102}^-$  clusters have the same geometry. Since we cannot make comparisons to other possible isomers at each cluster size, we do not present here the theoretical PES of these isomers. We remark, however, that except for  $\text{Al}_{102}^-$ , the PES corresponding to these clus-

TABLE VI. The same as Table I, but for the  $\text{Al}_{55}^-$  isomers. Additionally, the vertical ionization potentials (vIP) of the corresponding neutral clusters are given.

Isomer	$\Delta E$ (eV/K)	$E_g$ (eV)	vDE (eV)	vIP (eV)	$\langle d \rangle$ (Å)	$\delta_I$
55(1)	0.0	0.23	3.24	5.28	2.83	
55(2)	0.161/23	0.20	3.17	5.27	2.82	
55(3)	0.287/42	0.27	3.19	5.26	2.79	
55(4)	0.987/144	0.22	3.31	5.43	2.79	0.76
55(5)	1.060/155	0.30	3.35	5.33	2.81	
55(6)	1.553/227	0.27	3.29	5.31	2.80	0.81
55(7)	1.656/242	0.29	3.33	5.38	2.80	$\approx 1$

TABLE VII. Properties of  $\text{Al}_{52}^-$ ,  $\text{Al}_{54}^-$ ,  $\text{Al}_{79}^-$ , and  $\text{Al}_{102}^-$  fcc isomers: Binding energies per atom ( $E_b$ ), HOMO-LUMO gap ( $E_g$ ), vertical detachment energy (vDE), experimental detachment energy ( $\text{DE}^{\text{exp}}$ ), vertical ionization potential of the corresponding neutral isomer (vIP), experimental ionization potential ( $\text{IP}^{\text{exp}}$ ), and the mean nearest-neighbor distance ( $\langle d \rangle$ ). † denotes values determined from the PES threshold/value determined from location of the first peak of PES (when possible).

Isomer	$E_b$ (eV)	$E_g$ (eV)	vDE (eV)	$\text{DE}^{\text{exp}}$ (eV)†	vIP (eV)	$\text{IP}^{\text{exp}}$ (eV)	$\langle d \rangle$ (Å)
$\text{Al}_{52}^-$	3.20	0.12	3.20	2.95/3.05	5.67	5.18 <sup>a</sup> , 5.16 <sup>b</sup>	2.81
$\text{Al}_{54}^-$	3.21	0.15	3.08	2.92/2.98	5.42	5.18 <sup>a</sup> , 5.13 <sup>b</sup>	2.82
$\text{Al}_{79}^-$	3.26	0.05	3.24	3.36	5.14	5.15 <sup>b</sup>	2.84
$\text{Al}_{102}^-$	3.31	0.09	3.44	3.34/3.46	5.18	5.07 <sup>b</sup>	2.84

<sup>a</sup>From Ref. 6.

<sup>b</sup>From Ref. 41.

ters reproduce quite satisfactorily certain major features of experimentally measured spectra. The high fcc symmetry of these isomers is associated with degeneracies in the DOS, which may not be found in the experimental data. However, these effects might be reduced by including the thermal motion of the ions, which will reduce the high symmetry of these structures.

The average nearest-neighbor distance in these larger clusters essentially achieves the bulk value (see  $\langle d \rangle$  in Table VII). The value of the binding energy per atom,  $E_b$ , grows gradually when the cluster size increases reflecting a decrease in the ratio of surface to interior cluster atoms (see Table VII); at first glance, the value for  $\text{Al}_{102}^-$  seems to be quite close to the experimental fcc-bulk value 3.38 eV—this, however, is a fortuitous coincidence due to the overbinding resulting from LSD calculations.<sup>42</sup> The decrease with increasing cluster size of the HOMO-LUMO gap (see Table VII) may be interpreted also as an indication of the onset of bulk behavior.

Experimental electron detachment energies (DE) and ionization potentials (IP) for the clusters are also presented in Table VII. The experimental DE values were determined by either using the threshold value of the PES or by associating DE with the first peak of the PES (whenever such a peak is present). Most often, we find that the location of the first peak in the PES corresponds to the theoretical vDE value, and as seen from Table VII the theoretical vDE values are in rather good agreement with the experimental ones. The observation that the level of agreement between the calculated and measured values of vDEs is better than that between the calculated and measured PES (not shown) may reflect the high sensitivity of the PES to the specific isomeric structure of the cluster (and associated features in the DOS), while such dependence is weaker for electron detachment (vDE) or ionization (vIP) processes from larger clusters, due to the asymptotic nature of the electron detachment (or ionization) event.

## V. CONCLUSIONS

We have studied theoretically and experimentally the temperature-dependent photoelectron spectra of aluminum cluster anions. The theoretical method is based on LDA electronic-structure calculations and *ab initio* molecular-dynamics simulations, in conjunction with the use of the generalized Koopmans' theorem, which allows a direct con-

nection between the theoretically calculated electronic DOS and the experimental PES. Since the DOS is highly sensitive to structural changes of the cluster (that is, the arrangement of the ions), comparative studies of measured and calculated PES provide a very valuable method for determination of the structures of clusters. Furthermore, thermal effects in the PES can be addressed theoretically through averaging of the PES calculated along the dynamically evolving ionic trajectories generated via *ab initio* molecular-dynamics simulations at a selected temperature.

For  $\text{Al}_{19}^-$ ,  $\text{Al}_{20}^-$ , and  $\text{Al}_{23}^-$ , we trust that we have been able to determine the ground-state structures, as judged from the very good agreement between the experimental and the theoretical PES. For larger cluster sizes ( $N \geq 36$ ), the agreement was less satisfactory. This is most likely due to the complexity of the multidimensional energy surface. Nevertheless, by considering physically reasonable structural motifs for these cluster sizes, we were able to reproduce quantitatively certain signatures of shell closings exhibited in the measured PES.

The growth mechanism of Al clusters shows a change around  $N=20$  from the icosahedral<sup>13,14</sup> motif to the less strained decahedral and fcc-based motifs. This agrees qualitatively with findings of earlier *ab initio* studies.<sup>13,17-19</sup> In this study, we observed that for clusters with  $N > 20$ , significantly distorted fcc-resembling structures become energetically competitive with the decahedral ones. Furthermore, we demonstrated that the cubo-octahedron is a high-energy structure for a 55-atom fcc cluster because of its large (100) facets, which are characterized by a relatively large surface energy. Instead, the more likely growth motif consists of octahedral fcc structures,<sup>43</sup> where the cluster exposes mainly the (lower surface energy) close-packed (111) facets. Our results indicate that this fcc-octahedral motif should predominate as the size of the cluster increases, correlating with conclusions drawn from experiments for  $\text{Al}_N$  ( $N \geq 200$ ) clusters.<sup>44,45</sup>

## ACKNOWLEDGMENTS

Computations were performed on a Cray T3E at the Center for Scientific Computing, Espoo, Finland, and on an IBM RISC 6000/SP2 at the Georgia Tech Center for Computational Materials Science. Work in the University of Jyväskylä is supported by the Academy of Finland under the Finnish Center of Excellence Program 2000-2005 (Project No.

44875, Nuclear and Condensed Matter Program at JYFL). Work at Georgia Tech is supported by the U.S. DOE. The experimental work is supported by the NSF and performed at EMSL, a DOE user facility located at PNNL, which is oper-

ated for the DOE by Battelle Memorial Institute. L.S.W. acknowledges support from the Alfred P. Sloan Foundation. J.A. acknowledges discussions with S. Kümmel and wishes to thank the Väisälä Foundation for financial support.

- <sup>1</sup>W. A. de Heer, *Rev. Mod. Phys.* **65**, 611 (1993).
- <sup>2</sup>C. Yannouleas and U. Landman, in *Large Clusters of Atoms and Molecules*, edited by T. P. Martin (Kluwer, Dordrecht, 1996), p. 131.
- <sup>3</sup>W. Ekaradt, W.-D. Schöne, and J. M. Pacheco, in *Metal Clusters*, edited by W. Ekaradt (Wiley, Chichester, 1999), p. 1.
- <sup>4</sup>P. Ballone and W. Andreoni, in *Metal Clusters* (Ref. 3), p. 71.
- <sup>5</sup>H.-P. Cheng, R. N. Barnett, and U. Landman, *Phys. Rev. B* **48**, 1820 (1993).
- <sup>6</sup>K. E. Schriver, J. L. Persson, E. C. Honea, and R. L. Whetten, *Phys. Rev. Lett.* **64**, 2539 (1990); J. L. Persson, Ph.D. thesis, UCLA (1991).
- <sup>7</sup>W. A. de Heer, P. Milani, and A. Châtelain, *Phys. Rev. Lett.* **63**, 2834 (1989).
- <sup>8</sup>U. Ray, M. F. Jarrold, J. E. Bower, and J. S. Kraus, *J. Chem. Phys.* **91**, 2912 (1989).
- <sup>9</sup>K. J. Taylor, C. L. Pettiette, M. J. Craycraft, O. Chesnovsky, and R. E. Smalley, *Chem. Phys. Lett.* **152**, 347 (1988); G. Gantefor, K. H. Meiwes-Broer, and H. O. Lutz, *Phys. Rev. A* **37**, 2716 (1988); C. Y. Cha, G. Gantefor, and W. Eberhardt, *J. Chem. Phys.* **100**, 995 (1994); G. Gantefor and W. Eberhardt, *Chem. Phys. Lett.* **217**, 600 (1994).
- <sup>10</sup>X. Li, H. Wu, X.-B. Wang, and L.-S. Wang, *Phys. Rev. Lett.* **81**, 1909 (1998).
- <sup>11</sup>T. H. Upton, *Phys. Rev. Lett.* **56**, 2168 (1986); *J. Chem. Phys.* **86**, 7054 (1987).
- <sup>12</sup>R. O. Jones, *J. Chem. Phys.* **99**, 1194 (1993).
- <sup>13</sup>J. Akola, H. Häkkinen, and M. Manninen, *Phys. Rev. B* **58**, 3601 (1998).
- <sup>14</sup>J. Akola, M. Manninen, H. Häkkinen, U. Landman, X. Li, and L.-S. Wang, *Phys. Rev. B* **60**, R11 297 (1999).
- <sup>15</sup>B. K. Rao and P. Jena, *J. Chem. Phys.* **111**, 1890 (1999).
- <sup>16</sup>V. Kumar, *Phys. Rev. B* **57**, 8827 (1999); V. Kumar, S. Bhattacharjee, and Y. Kawazoe, *ibid.* **61**, 8541 (2000).
- <sup>17</sup>J.-Y. Yi, D. J. Oh, and J. Bernholc, *Chem. Phys. Lett.* **174**, 461 (1990); *Phys. Rev. Lett.* **67**, 1594 (1991).
- <sup>18</sup>H.-P. Cheng, R. S. Berry, and R. L. Whetten, *Phys. Rev. B* **43**, 10 647 (1991).
- <sup>19</sup>S. H. Yang, D. A. Drabold, J. B. Adams, and A. Sachdev, *Phys. Rev. B* **47**, 1567 (1993).
- <sup>20</sup>R. N. Barnett and U. Landman, *Phys. Rev. B* **48**, 2081 (1993).
- <sup>21</sup>D. J. Tozer and N. C. Handy, *J. Chem. Phys.* **108**, 2545 (1998); **109**, 10 180 (1998).
- <sup>22</sup>N. Binggeli and J. R. Chelikowsky, *Phys. Rev. Lett.* **75**, 493 (1995).
- <sup>23</sup>C. Massobrio, A. Pasquarello, and R. Car, *Phys. Rev. Lett.* **75**, 2104 (1995); *Phys. Rev. B* **54**, 8913 (1996).
- <sup>24</sup>L. S. Wang, H. S. Cheng, and J. Fan, *J. Chem. Phys.* **102**, 9480 (1995); L. S. Wang and H. Wu, in *Advances in Metal and Semiconductor Clusters. IV. Cluster Materials*, edited by M. A. Duncan (JAI Press, Greenwich, 1998), p. 299.
- <sup>25</sup>L. S. Wang and X. Li, *Temperature Effects in Anion Photoelectron Spectroscopy of Metal Clusters*, in *Proceedings of the International Symposium on Clusters and Nanostructure Interfaces, Richmond, 1999*, edited by P. Jena, S. N. Khanna, and B. K. Rao (World Scientific, River Edge, New Jersey, 2000).
- <sup>26</sup>S. H. Vosko, L. Wilk, and M. Nusair, *Can. J. Phys.* **58**, 1200 (1980); S. H. Vosko and L. Wilk, *J. Phys. C* **15**, 2139 (1982).
- <sup>27</sup>N. Troullier and J. L. Martins, *Phys. Rev. B* **43**, 1993 (1991). For the aluminum  $3s^23p^1$  valence electrons, we use  $s$ -nonlocal and  $p$ -local components with cutoff radii of 2.1 and  $2.5a_0$ , respectively. The KS orbitals are expanded in a plane-wave basis with a cutoff of 15.4 Ry.
- <sup>28</sup>J. P. Perdew, K. Burke, and M. Ernzerhof, *Phys. Rev. Lett.* **77**, 3865 (1996); **78**, 1396(E) (1997).
- <sup>29</sup>K. W. Jacobsen, J. K. Nørskov, and M. J. Puska, *Phys. Rev. B* **35**, 7423 (1987).
- <sup>30</sup>The Monte Carlo fcc-generation procedure consists of the following steps: First an fcc lattice is generated inside a sufficiently large sphere with the lattice sites randomly populated. Next, occupied sites are varied according to the Metropolis algorithm using the average coordination number per atom as the cost function and a certain mobility-parameter (“temperature”). The mobility of atoms is gradually decreased in conjunction with the iterative maximization of the coordination number. In order to avoid local minima, the procedure is repeated several times. By construction, this procedure favors formation of (111) facets at the surface of the cluster.
- <sup>31</sup>J. F. Janak, *Phys. Rev. B* **18**, 7165 (1978).
- <sup>32</sup>J. Akola, H. Häkkinen, and M. Manninen, *Eur. Phys. J. D* **9**, 179 (1999).
- <sup>33</sup>J. P. Perdew *et al.*, *Phys. Rev. Lett.* **49**, 1691 (1982); J. P. Perdew and M. Levy, *ibid.* **51**, 1884 (1983); S. B. Trickey, *ibid.* **56**, 881 (1986); J. P. Perdew and K. Burke, *Int. J. Quantum Chem.* **57**, 309 (1996); M. Harris and P. Ballone, *Chem. Phys. Lett.* **303**, 420 (1999).
- <sup>34</sup>J. Akola, A. Rytönen, H. Häkkinen, and M. Manninen, *Eur. Phys. J. D* **8**, 93 (2000).
- <sup>35</sup>The eigenvalues of the inertia tensor are considered (nearly) degenerate if the values are within 5% from each other.
- <sup>36</sup>In Fig. 4 we have used the mean value of  $v_{xc}^\infty = 1.47$  eV calculated for the whole set of our  $Al_{20}^-$  isomers. The  $v_{xc}^\infty$  value of the 20(1) isomer is 0.08 eV higher, which is a deviation that is atypical for the  $Al_{20}^-$  isomers. The mean value, however, seems to be appropriate for all the inner KS states (see Fig. 4) but may underlie the observed disagreement for the locations of the calculated and measured lowest-energy peak of the PES of 20(1). We also note that the charge-density isosurface of the HOMO state of the 20(1) isomer (see Fig. 5) is mostly localized in the vicinity of the two outermost atoms along the long deformation axis of the cluster. The orbital character of this state differs clearly from that of the underlying states where the orbital charge is more delocalized over the whole cluster.
- <sup>37</sup>I. Hamamoto, B. Mottelson, H. Xie, and X. Z. Zhang, *Z. Phys. D: At., Mol. Clusters* **21**, 163 (1991).
- <sup>38</sup>S. M. Reimann, M. Koskinen, H. Häkkinen, P. E. Lindelöf, and

- M. Manninen, Phys. Rev. B **56**, 12 147 (1997).
- <sup>39</sup>A. Rytönen, H. Häkkinen, and M. Manninen, Phys. Rev. Lett. **80**, 3940 (1998).
- <sup>40</sup>Note that these “pockets” seem to form a ring or a torus along the perimeter of the slightly oblate cluster. This indicates that the corresponding wave function has a sixfold nodal structure with respect to a rotation about the axis normal to the above-mentioned ring (see Fig. 9, perpendicular to the plane of the paper). In the jellium model this would correspond to an  $(l, m) = (6, \pm 6)$  state.
- <sup>41</sup>M. Pellarin, B. Baguenard, M. Broyer, J. Lermé, and J. L. Vialle, J. Chem. Phys. **98**, 944 (1993).
- <sup>42</sup>In the range of cluster sizes considered here, the GGA correction (Ref. 28) tends to lower the binding energy per atom by 0.3–0.4 eV, bringing our earlier LSD results (Ref. 13) to closer agreement with the measured photodissociation data (Ref. 8).
- <sup>43</sup>S. Valkealahti, U. Näher, and M. Manninen, Phys. Rev. B **51**, 11 039 (1995).
- <sup>44</sup>T. P. Martin, U. Näher, and H. Schaber, Chem. Phys. Lett. **199**, 470 (1992).
- <sup>45</sup>U. Näher, U. Zimmermann, and T. P. Martin, J. Chem. Phys. **99**, 2256 (1993).